

The Use of Passive Magnetic Methods in Inferring the Variability of Sub-Glacial Water Systems

Nicholas Hac

Advisor: Jeremy Bassis, PhD

09/14/2011

1 Abstract

Over the past few decades, glaciers worldwide have been retreating, resulting in changes in water resources with direct socio-environmental impacts. The flow of glaciers is intrinsically linked to the morphology and dynamics of sub-glacial water. However, these sub-glacial processes remain largely mysterious, and current techniques of modeling the glacial flow based on these sub-glacial structures is limited to theoretical models with few direct observations of sub-glacial water. Current techniques of observing sub-glacial water systems, including satellite altimetry, boreholes, and active source geophysics, are limited either spatially or temporally. In this study, we present the plausibility of using passive magnetic methods, including magnetic induction and magneto-tellurics, using natural external magnetic fields to detect sub-glacial water morphology and dynamics. Magnetic induction alone was found useful in detecting the presence of smaller bodies of water, but only the variability of large lake-like bodies of sub-glacial water. Magnetotellurics was proven more useful in detecting the presence of smaller bodies of water. We constructed several forward models using these techniques, and calculations of both novel potential measurements and notes on the limitations of these techniques have been made.

2 Introduction

A wealth of research over the past several decades has reliably shown that glaciers are retreating worldwide (Kaser et al. 2006). As a result, global sea levels are rising, and assuming the change in global climate trends continue, levels are predicted to continue rising over the years (Arendt et al., 2002). Thus, it is imperative to predict the extent of worldwide glacial retreating, thereby predicting the extent of this sea level rise over the centuries.

The morphology and dynamics of sub-glacial water systems have been convincingly shown to be linked with the dynamics of glacial movement (Kamb, 1970; Iken, 1981; Kamb, 1987; Iken and Bindshadler, 1986; Zwally et al., 2002; Stearns et al., 2008; Das et al., 2008). Numerous researchers have posited to predict these glacial dynamics using models based on a wide range of spacial and temporal sub-glacial water dynamics. For example, the sub-glacial water systems may transition from an evenly distributed thin sheet of water to a channelized water system over the course of a season (e.g. Gordon et al., 1998; Stearns et al., 2008), thus influencing the glacial movement. However, as a result of the temporal and spacial variability of these water systems and the depth of these systems beneath glaciers, it is difficult to directly observe the dynamics of sub-glacial water systems. Thus, the actual nature of these systems have eluded scientists. Since many of these systems are a kilometer or more below the surface of glaciers, direct measurements are few, and predictions of the exact influence of sub-glacial water systems on glacial movement is largely limited to theoretical models (e.g. Fowler, 1979; Fowler, 1986), as the scarcity of actual data greatly limits experimental models.

The existing methods of observing sub-glacial water systems are limited in scope, unable to resolve both spatial and temporal variability of these networks. Satellite altimetry may be employed to take snap-shots of glaciers over large spatial coordinates. Given the active nature of these measurements and the infrequency of the snap-shots taken, these images cannot be resolved over short time frames. Active source geophysics, in which a signal is artificially injected into the Earth to infer a seismic profile, is costly and may be damaging to the glacial structure. Thus, it is also unrealistic as a tool for temporal resolution, although it may be spatially effective. Boreholes are field-based measurements that are practical for resolving the dynamics of these water systems over time, but they are very limited spatially, as the expense of drilling boreholes across large swaths of glacier is large. In this

study, we explore two techniques, magnetic induction and magneto-tellurics, that may be used to resolve the dynamics of sub-glacial water systems both spatially and temporally.

The first of these techniques is the use of passive magnetic induction alone. The use of magnetics has potential in detecting the amount of water below the surface of a glacier since water is far more conductive than ice and oftentimes more conductive than bedrock as well. By using the magnetic fields naturally produced from Earth's ionosphere, we may be able to study the evolution of sub-glacial water systems. Furthermore, since the measurements are made passively, using common magnetometers, the technique may be very cost effective. Although promising, this technique has not been widely used to detect underground water or any other conductive underground source in a sub-glacial environment. This technique has been used, however, as strong evidence that a planet-wide ocean exists beneath the surface of Europa, an icy moon that orbits Jupiter (Zimmer et al. 2000), and its use in detecting the dynamics of sub-glacial water is, therefore, worth exploring.

The second method is the use of magneto-tellurics, which may be useful in detecting the dynamics of sub-glacial water. This technique involves the detection of not only the natural magnetic field but also the natural electric field at the surface of the Earth, and is thus more costly, albeit more informative, than the above technique of measuring the magnetic induction alone. However, since these detections are also done passively, this technique is still potentially more cost effective than currently used techniques. Since magneto-tellurics is widely used in hydrocarbon and mining exploration, geothermal investigation, and groundwater monitoring (Orange, 1989; Farquharson and Craven, 2009; Volpi et al., 2003; Pedersen et al., 2005), it is promising in detecting sub-glacial water.

3 Theory and Models

Here we introduce the basic theory of both magnetic induction and magneto-tellurics, each of which are promising techniques, which may potentially be used to detect the presence and variability of sub-glacial water systems to different extents. Figure 1 illustrates the general structure of the glacier, sub-glacial water, and bedrock system we visualize for the following results. The water layer will not necessarily be completely flat. Its

morphology is variable. We use forward models to calculate how various water system structures will affect the data in both magnetic induction and magneto-telluric calculations. The theory, models, and significant results are presented below.

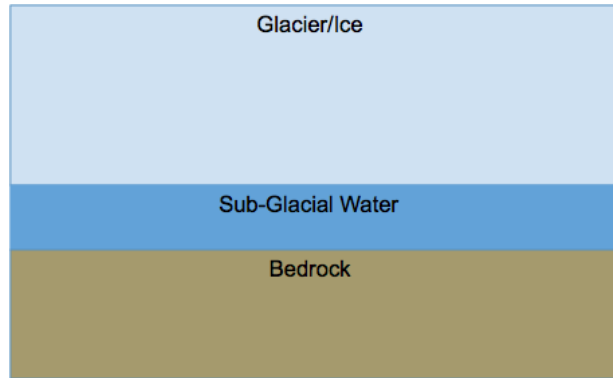


Figure 1: This figure illustrates the general structure of the glacier, sub-glacial water, and bedrock system we visualize for the following results. The water layer will not necessarily be completely flat. Its morphology is variable.

3.1 Magnetic Induction Theory

Unlike traditional magnetic surveys which rely on measuring the static magnetic fields based on the internal magnetization of sub-glacial water systems to infer their structure, magnetic induction relies on the time and space varying magnetic fields that result from a known external magnetic field. This technique may be implemented passively because these external magnetic fields may be natural fields produced by the Earth. The costs associated with such an undertaking result from the deployment of magnetometers along the glacial surface for an extensive period of time (from days to years) in order to gather enough magnetic data to infer sub-glacial structure and variability. Since most magnetometers can detect changes in the magnetic field on the order of 1 nT or higher, the sources used would need to exhibit variations on this order or higher. Natural variations in Earth's magnetic field include variations occurring each second on the order of 1 - 10 nT, diurnal variations on the order of 10 - 100 nT, and the large magnetic storms that vary on the order of 100 - 1000 nT (Stepisnik, 2006).

It is well known that water, particularly water containing dissolved salts, is much more conductive than ice. Typical drinking water and freshwater has a conductivity on the order of $0.01 - 1$ S/m. Seawater, on the other hand, has a conductivity around $1 - 6$ S/m (Cox et al., 1970). However, ice has a conductivity on the order of $10^{-6} - 10^{-5}$ S/m (Kulesa, 2007). Thus, there is a large contrast between the conductivities of water and ice. The conductivity of bedrock is typically on the order of $10^{-4} - 10^{-3}$ S/m (Seaton and Dean, 2004). The contrast between the conductivities of bedrock and water is often large, although not always, and is thus sometimes an important limit in measurements.

Conceptually, an external time-varying magnetic field will induce an electromotive force in a closed circuit. This is a statement of the well-known Faraday’s law, which relates the electric field with the external magnetic field as such:

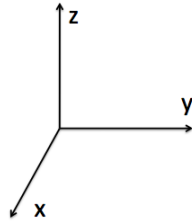
$$\nabla \times \mathbf{E} = -\frac{\partial \mathbf{B}}{\partial t} \quad (1)$$

where we note that the bold-face means these are vectors. In the water, this electric field is in the form of eddy currents. Due to water’s high conductivity, the eddy currents in water are far more significant than the eddy currents in ice or bedrock. These eddy currents, in turn, induce a magnetic field that acts opposite the change in the external magnetic field, partially canceling the external field. Extricating this induced field from the external field contains the information about the sub-glacial environment.

The best way to find out the potential use of this method is to calculate the ratio of the induced magnetic field over the external magnetic field. Any measurement taken over seconds may only be detected if this ratio is between 0.1 - 1 since, as stated earlier, the Earth’s magnetic field varies each second on the order of $1 - 10$ nT and magnetometers can changes on the order of 1 nT. Likewise, day-long periods can detect changes with a ratio as low as 10^{-2} , and magnetic storms, which are periods on the order of hours, can measure changes with a ratio as low as 10^{-3} . We use forward models to calculate what effects certain water structures would have on the ratio of the induced magnetic field over the external magnetic field.

3.2 Magnetic Induction Results

We can mathematically represent various water system structures by first assuming the structure is a conducting sheet lying in a plane, similar to the structure shown in Figure 1, say at $z = 0$ in Cartesian coordinates, where we use the convention presented below:



Price (1949) originally derived the general equation for a non-uniform conducting plane sheet as presented below:

$$-\rho \left(\frac{\partial^2 \Omega^{(i)}}{\partial z^2} \right) + \nabla \rho \nabla \Omega^{(i)} + \frac{\partial}{\partial t} \left(\frac{\partial \Omega^{(i)}}{\partial z} \right) = -\frac{\partial}{\partial t} \left(\frac{\partial \Omega^{(e)}}{\partial z} \right) \quad (2)$$

where ρ is a dimensionless resistance explained below, $\Omega^{(i)}$ is induced magnetic potential, $\Omega^{(e)}$ is external magnetic potential, and z is the axis normal to the ground and is, thus, the axis measuring the depth of the water. We note that ρ , the dimensionless resistance of the following form:

$$\rho = \frac{1}{\mu_0 \sigma d(x)} \quad (3)$$

where μ_0 is the vacuum permeability, σ is the conductivity of water, and $d(x)$ is the depth of the water layer, which we note may depend on the distance of the water layer along the x -axis. The relationship between the magnetic potential (scalar) and the magnetic field is:

$$\mathbf{B} = -\nabla \Omega \quad (4)$$

where \mathbf{B} is the vector magnetic field. Finally, we note that we can represent the induced and external magnetic potentials as:

$$\Omega^{(i)} = b e^{i\omega t} f(x, y) e^{-kz} \quad (5)$$

$$\Omega^{(e)} = Fe^{i\omega t}g(x, y)e^{kz} \quad (6)$$

where b and F are the amplitudes of the induced and external magnetic fields respectively, ω is the frequency of the field, $f(x, y)$ and $g(x, y)$ are functions dependent on x and y , but not z , and k is the inverse of wavelength, λ^{-1} .

With equation (2) in mind, we are now able to illustrate the plausibility of detecting sub-glacial water by modeling various morphologies of the sub-glacial water structure. Below, we illustrate three different structures. We begin by modeling the simple flat water layer model, in which the water has a constant depth throughout the entire x - y coordinate plane to see what combinations of depths and conductivities may be measured. Second, we model a water layer with a depth that varies sinusoidally along the x -axis, representing a more channeled water layer to gauge our ability to measure this variation. Finally, we model an individual Gaussian channel to evaluate the possibility of detecting individual channels. In all models, we treat the ice and bedrock as complete insulators, a reasonable assumption only when the bedrock is around at least three orders of magnitude more conductive than water. There is an important limitation to this assumption. Since the bedrock is assumed to have infinite depth, the induced magnetic field should completely cancel with the external magnetic field even if the bedrock slightly conducts. In practice, this is solved by using multiple magnetometers on the surface of the Earth arranged at angles. However, we make the above approximations to find the baseline parameters of sub-glacial water systems to detect their presence and variability.

3.2.1 Flat Water Layer Model

The flat water layer model is the simplest model used to quantify the potential to detect water using the magnetic induction method. It is a model that treats the ice and bedrock as perfect insulators, whereas the water is treated as a flat, infinite sheet of constant depth and conductance across the whole x - y plane. In this model, since we treat the depth as a constant, the unit-less resistance ρ is also constant:

$$\rho = \frac{1}{\mu_0\sigma d} \quad (7)$$

where d is a constant independent of x . Inserting (5), (6), and (7) into (2), we find:

$$(\rho k^2 + i\omega k)\Omega^{(i)} = i\omega k\Omega^{(e)} \quad (8)$$

Rearranging, we obtain the ratio of $\Omega^{(i)}$ to $\Omega^{(e)}$:

$$\frac{\Omega^{(i)}}{\Omega^{(e)}} = \frac{i\omega\mu\sigma d\lambda}{1 + i\omega\mu\sigma d\lambda} \quad (9)$$

By examining (5), (6), and (9), we note that:

$$\left| \frac{b}{F} \right| = \left| \frac{i\omega\mu\sigma d\lambda}{1 + i\omega\mu\sigma d\lambda} \right| \quad (10)$$

where b is the amplitude of the induced magnetic field and F is the amplitude of the external magnetic field.

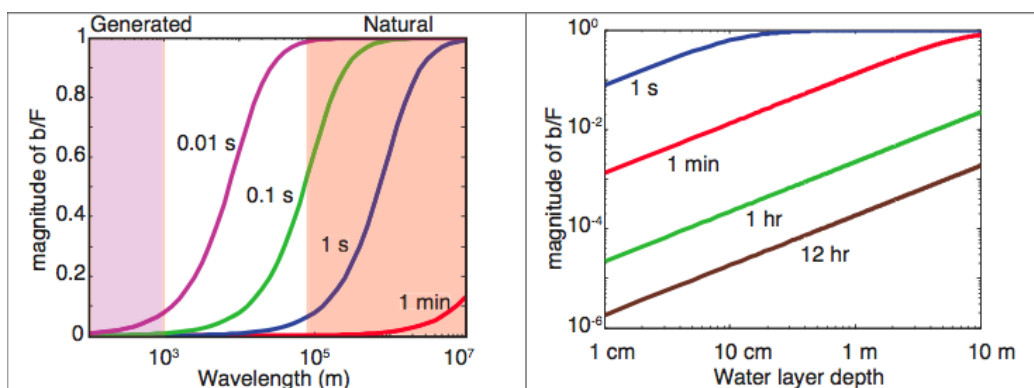


Figure 2: The graph on the left shows the magnitude of the ratio of the induced magnetic field to the external magnetic field as a function of the external wavelength for a total water conductivity of 0.1 S given a range of periods. The external wavelength is typically on the order of an Earth radius, or around $10^6 - 10^7$ m . It can also be on the order of 10^5 m . The graph on the right shows the magnitude of the ratio of the induced magnetic field to the external magnetic field as a function of water depth for a conductivity of 0.1 S/m and external wavelength of 10^7 m .

Figure 2 above shows some basic results using equation (10). The graph on the left shows the magnitude of the ratio of the induced magnetic field to the external magnetic field as a function of the external wavelength for a total water conductivity of 0.1 S given a range of periods. The orange region on the right shows the range of wavelengths naturally produced by Earth's ionosphere. The purple region on the left shows the wavelengths that would have to be artificially produced. The graph on the right shows the magnitude of the ratio of the induced magnetic field to the external magnetic field as a

function of water depth for a conductivity of 0.1 S/m and external wavelength of 10^7 m . Recalling that we like the ratio of b to F to be on the order of 10^{-1} , we note shorter period external fields are more sensitive to shallower water layers. The above table presents promising results. We note that water layers on the order of a centimeter can realistically be detected by 1 s periods. Deeper water layers can be detected using naturally-varying external fields of longer periods. Magnetometers can easily detect variations of the order of seconds or more. Thus, when it comes to detecting the presence of water itself, passive techniques are sufficient when detecting thin water layers of a centimeter or more.

3.2.2 Sinusoidal Layer Model

The sine-varying layer model is the simplest model we use in order to quantify the potential to detect variabilities in water layer structure. It is a model that again treats the ice and bedrock as perfect insulators. However, the water layer now has a depth varying periodically. In this model, the unit-less resistance ρ is:

$$\rho(x) = \rho_0(1 - \epsilon \cos px) \quad (11)$$

where $\rho_0 = (\mu_0 \sigma d_{max})^{-1}$ and p is the inverse wavelength of the variability in the water layer. Using this periodic model, Price (1949) showed that given an external magnetic potential where:

$$g(x, y) = \cos ky \quad (12)$$

and specifying a new form of (6) such that:

$$\Omega^{(e)} = F e^{i\omega t} \cos ky e^{kz} \quad (13)$$

the induced magnetic potential from (5) can be written:

$$\Omega^{(i)} = \cos ky \sum_{m=0}^{\infty} I_m e^{i\omega t} \cos mpx e^{-z\sqrt{k^2+m^2p^2}} \quad (14)$$

where I_m are the coefficients in a Fourier series. We must solve for the recurrence relationships among the coefficients. We start by solving for the first coefficient, I_0 and ignoring the rest. We insert (11), (13), and (14) into (2) to get:

$$\rho_0(1 - \epsilon \cos px) \cos ky e^{i\omega t} k^2 I_0 e^{-kz} + i\omega \cos ky e^{i\omega t} k I_0 e^{-kz} = i\omega \cos ky e^{i\omega t} k F e^{kz} \quad (15)$$

which, when simplified and rearranging to find the ratio of the first coefficient of the Fourier series of the induced magnetic potential to the magnitude of the external magnetic potential, we get:

$$\left| \frac{I_0}{F} \right| = \left| \frac{i\omega}{k\rho_0(1 - \epsilon \cos px) + i\omega} \right| \quad (16)$$

To check that the above is correct, we note that when $\epsilon = 0$, (16) reduces to (10). Next, we find the relationship between I_1 and I_0 by applying (14) with only these first two coefficients, ignoring all higher order terms, to (2) to get:

$$k^2 \rho_0 I_0 + i\omega k I_0 + (-\epsilon k^2 \rho_0 I_0 + \zeta^2 I_1 + i\omega \zeta I_1) \cos px - \epsilon \zeta^2 \rho_0 I_1 \cos^2 px + \epsilon p^2 \rho_0 I_1 \sin^2 px = i\omega k F \quad (17)$$

where $\zeta^2 = k^2 + p^2$. In order to find the relationship between I_0 , I_1 and F , we convert the trigonometric functions into complex form, then take those terms that are independent of x and rearrange, obtaining:

$$\frac{\epsilon}{2} I_1 = (1 + D) I_0 - DF \quad (18)$$

where $D = \frac{i\omega}{\rho_0 k}$. Using a similar approach, we may return to (14) and add in I_2 (while neglecting all higher order terms) such that we may find the relationship between I_0 , I_1 , and I_2 . Once we use this form of (14) up to $m = 2$ in (2), we may once again take those terms independent of x and rearrange to get back (18). By taking those terms dependent on e^{ipx} and e^{-ipx} , we attain the following relationship between I_0 , I_1 , and I_2 :

$$\epsilon \left(s + \frac{1}{2} \right) I_2 = (s + 1) [1 + (s + 1)^{-\frac{1}{2}} D] I_1 - \epsilon I_0 \quad (19)$$

As we subsequently add terms to the sum in (14), then solve for the terms independent of x , we get back (18). By solving for those terms dependent on e^{ipx} and e^{-ipx} , we get back (19). By solving for terms dependent on higher order terms, e^{impx} and e^{-impx} , we find the following generalized recurrence relationship:

$$\frac{\epsilon(m+1)ms+1}{2m(m-1)s+1}I_{m+1} = \frac{m^2+1}{m(m-1)s+1} \left[1 + \frac{D}{\sqrt{m^2s+1}} \right] I_m - \frac{\epsilon}{2}I_{m-1} \quad (20)$$

thus giving us a series of linear equations which may easily be solved.

Figure 3 on the next pages shows the ratio of the magnitude of the first and second Fourier series coefficients (labeled b) to the magnitude of the external magnetic field, F , in this sinusoidal model. The blue curves represent a 1 km wide “wavelength” of the sinusoidal water depth. The green curves represent a 10 km wide variability and the red curves represent a 100 km wide variability. The above graphs assume 10^5 m wavelength of the external magnetic field and 0.1 S conductivity. The rationale for using this conductivity is that it is common for freshwater systems on the order of 1 m deep, and sometimes even 10 cm deep. The first coefficient is useful for informing us of the presence of water. The second coefficient is useful for informing us of the variability in the water. As can be seen from Figure 2, the more macroscopic variabilities covering larger swaths of land give larger magnitudes for the ratio of the second Fourier series coefficient to the amplitude of the external magnetic field. Although in all cases, it is relatively straightforward to detect the presence of the water, detecting the actual variability in the water is more difficult. Recalling that we like the ratio of b to F to be on the order of 10^{-1} , we note only when we have a water layer with the huge 100 km wavelength in variability are we able to easily detect this variability. One order of magnitude less and might need the variability in a magnetic storm to detect this variability.

With (18), (19), and (20) available to us, we take this time to investigate the possibility of using artificial generated external magnetic fields to detect the presence and variability of subglacial water systems. Figure 4 shows the ratio of the magnitude of the first and second Fourier series coefficients (labeled b) to the magnitude of the external magnetic field, F , in the sinusoidal model. The blue curves represent a 10 m wide “wavelength” of the sinusoidal water depth. The green curves represent a 100 m wide variability and the red curves represent a 1 km wide variability. The above graphs assume 10^2 m wavelength of the artificially generated external magnetic field and 0.1 S water conductivity. When the artificially generated external magnetic field is at much shorter wavelengths than those of the natural magnetic fields in Earth’s ionosphere, and when these fields are produced at very short periods, much smaller variabilities in the sub-glacial water may be detected. Such an

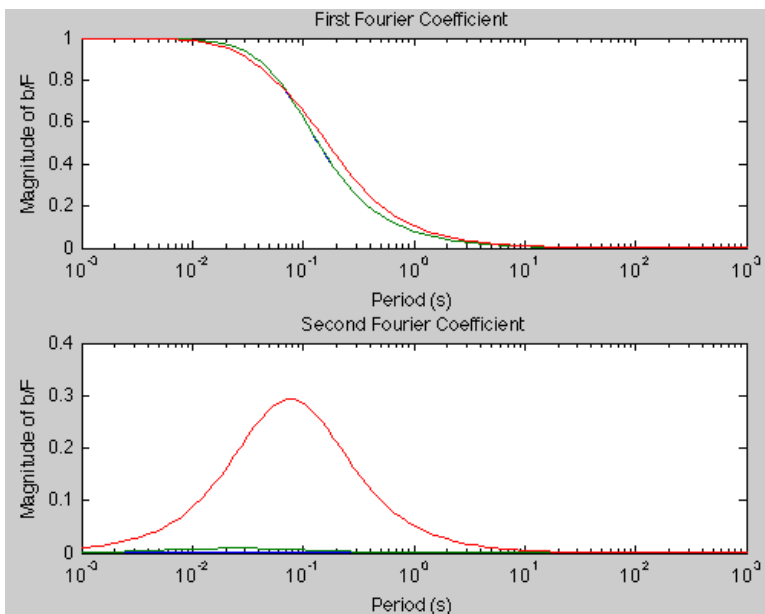


Figure 3: The above graphs show the ratio of the magnitude of the first and second Fourier series coefficients (labeled b) to the magnitude of the external magnetic field, F , in the sinusoidal model. The blue curves represent a 1 km wide "wavelength" of the sinusoidal water depth. The green curves represent a 10 km wide variability and the red curves represent a 100 km wide variability. The above graphs assume 10^5 m wavelength of the external magnetic field and 0.1 S water conductivity.

undertaking would be significantly more costly than using passive techniques. However, if it turns out there is a feasible, affordable way to generate this artificial field, then detecting the variability in sub-glacial water systems will be straightforward with magnetic methods alone.

3.2.3 Gaussian Channel Model

The Gaussian model is the simplest model we use in order to quantify the potential to detect the size of an individual water channel. It is, once again, a model that treats the ice and bedrock as perfect insulators, whereas the resistivity of the water is treated as a single channel in the shape of a Gaussian with a very thin resistivity going out to infinity. In this model, we treat the unit-less resistance ρ as:

$$\rho(x) = \rho_0 \left(1 - \sum_{n=1}^{\infty} \epsilon_n \cos npx \right) \quad (21)$$

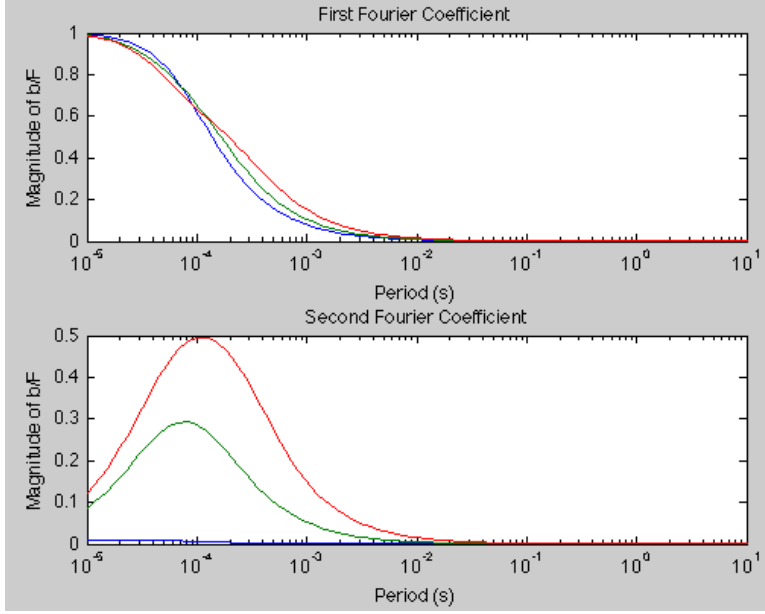


Figure 4: The above graphs show the ratio of the magnitude of the first and second fourier series coefficients (labeled b) to the magnitude of the external magnetic field in the sine-varying layer model. The blue curves represent a 10 m wide "wavelength" of the sinusoidal water depth. The green curves represent a 100 m wide variability and the red curves represent a 1 km wide variability. The above graphs assume 10^2 m wavelength of the artificially generated external magnetic field and 0.1 S water conductivity.

where ρ_0 is the same as in the previous model, $\epsilon_1 \leq \rho_0$ and all subsequent values of ϵ_n satisfy the following relationship with ϵ_1 :

$$\epsilon_n = \epsilon_1 e^{-2\pi(k\alpha(n-1))^2} \quad (22)$$

where α is a measure of the channel's thickness. It can be thought of as the standard deviation of the Gaussian shape, or the standard deviation of water resistivity from the center-point. We notice that if we attempt to plug (13), (14), and (21) into (2), we must end up with a recurrence within a recurrence since there are two infinite sums. Instead of attempting to solve for this double recurrence, we will explicitly and analytically solve for the induced magnetic potential (14) for the first 5 terms, dropping off all remaining terms, and the first 4 terms in the unit-less resistance (21) such that we end up with the following approximations:

$$\Omega^{(i)} \approx \cos ky \sum_{m=0}^4 I_m e^{i\omega t} \cos mpx e^{-z\sqrt{k^2+m^2p^2}} \quad (23)$$

$$\rho(x) \approx \rho_0 \left(1 - \sum_{n=1}^4 \epsilon_n \cos npx \right) \quad (24)$$

By explicitly plugging (13), (23), and (24) into (2), we obtain a series of terms, some of which are independent of x , and some of which are dependent on $\cos px$, $\cos 2px$, $\cos 3px$, or $\cos 4px$. By extracting the appropriate dependencies, we may find the relationships among all the terms in (23) and (24). By finding all of these relationships, we come up with the following 5 linear equations, which may easily be solved:

$$(1 + D)I_0 - \frac{\epsilon_1}{2}I_1 - \frac{\epsilon_2}{2}I_2 - \frac{\epsilon_3}{2}I_3 - \frac{\epsilon_4}{2}I_4 = DF \quad (25)$$

$$\begin{aligned} & -\epsilon_1 I_0 + \left(1 + s + D\sqrt{1+s} - \frac{\epsilon_2}{2}(1-s) \right) I_1 \\ & \quad - \left(\frac{\epsilon_1}{2}(1+2s) + \frac{\epsilon_3}{2}(1-2s) \right) I_2 \\ & - \left(\frac{\epsilon_2}{2}(1+3s) + \frac{\epsilon_4}{2}(1-3s) \right) I_3 - \left(\frac{\epsilon_3}{2}(1+4s) \right) I_4 = 0 \end{aligned} \quad (26)$$

$$\begin{aligned} & -\epsilon_2 I_0 - \left(\frac{\epsilon_1}{2}(1+2s) + \frac{\epsilon_3}{2}(1-2s) \right) I_1 \\ & + \left(1 + 4s + D\sqrt{1+4s} - \frac{\epsilon_4}{2}(1-4s) \right) I_2 \\ & - \left(\frac{\epsilon_1}{2}(1+6s) \right) I_3 - \left(\frac{\epsilon_2}{2}(1+8s) \right) I_4 = 0 \end{aligned} \quad (27)$$

$$\begin{aligned} & -\epsilon_3 I_0 - \left(\frac{\epsilon_2}{2}(1+3s) + \frac{\epsilon_4}{2}(1-3s) \right) I_1 - \left(\frac{\epsilon_1}{2}(1+2s) \right) I_2 \\ & + \left(1 + 9s + D\sqrt{1+9s} \right) I_3 - \left(\frac{\epsilon_1}{2}(1+12s) \right) I_4 = 0 \end{aligned} \quad (28)$$

$$\begin{aligned} & -\epsilon_4 I_0 - \left(\frac{\epsilon_3}{2} \right) I_1 - \left(\frac{\epsilon_2}{2}(1+8s) \right) I_2 - \left(\frac{\epsilon_1}{2}(1+12s) \right) \\ & \quad + \left(1 + 16s + D\sqrt{1+16s} \right) I_4 = 0 \end{aligned} \quad (29)$$

We solve for (25) - (29) under varying conditions of water depth, conductivity, and width of channel.

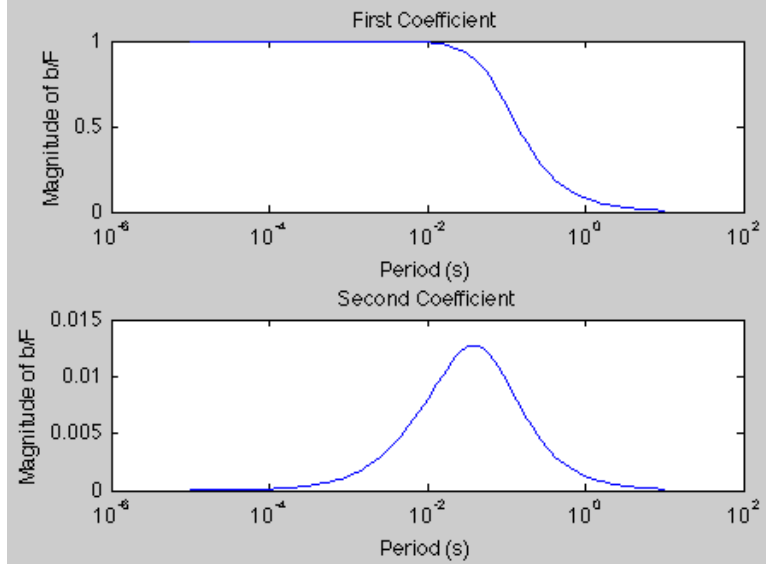


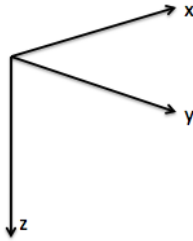
Figure 5: The above graphs show the ratio of the magnitude of the first and second Fourier series coefficients (labeled b) to the magnitude of the external magnetic field, F , in the Gaussian single channel model. The blue curve represents a 10 km wide channel. The above graphs assume 10^5 m wavelength of the external magnetic field and 0.1 S water conductivity.

Figure 4 shows the ratio of the magnitude of the first and second Fourier series coefficients (labeled b) to the magnitude of the external magnetic field, F , in the Gaussian single channel model. The blue curve represents a 10 km wide channel. The above graphs assume 10^5 m wavelength of the external magnetic field and 0.1 S water conductivity. Gaussian channels that are even an order of magnitude smaller have a second Fourier coefficient that are too small to detect. Similar to the sinusoidal curve, although detecting the presence of the water itself is straightforward, detecting the variability in the water to find that it is a channel is very difficult. Even with a 10 km wide channel, this ratio between the induced and external magnetic potential is less than the desire 10^{-1} . Thus, we would something passive with a magnitude on the order of a magnetic storm to accurately detect this variability.

3.3 Magneto-tellurics Theory

Unlike the magnetic induction method, which detects natural changes in the magnetic field, the magneto-telluric method relies on the detection of the magnetic and electric components of static telluric currents at Earth's surface. These telluric currents are naturally present at a range of frequencies in Earth's crust, and may be detected at the surface. By measuring the ratio of the amplitudes of the electric field to the magnetic field, we determine information on the apparent resistivity of the subsurface of the Earth, where this apparent resistivity is a weighted average of the resistivities of the various layers of material below the surface. By measuring this ratio at a range of frequencies, we can determine a profile of the structure below the surface. By also measuring the phase shift between the electric and magnetic fields at various frequencies, we can determine a more accurate profile for verification purposes, although phase shifts are not discussed below. Because the resistivities of ice, bedrock, and water are all so different from one another, this technique is promising as a method for finding out their relative structures and depths below the surface.

Combining both the magnetic and electric data, we can obtain more information about the sub-glacial water system. As originally proposed by Louis Cagniard in the early 1950s, we illustrate the mathematics needed to understand the theory behind magneto-tellurics. For the following, we will use the following convention for axes:



where z is positive as we descent vertically. Let us suppose we have a layer of Earth lying along the plane $z = 0$ with infinite depth and constant conductivity σ . Let us also suppose the electric field is moving along the z -axis with an amplitude running along the x -axis. Thus, the magnetic field is moving along the z -axis with its amplitude running along the y -axis. We will first consider the current density of the electric field:

$$\mathbf{J} = \sigma \mathbf{E} \quad (30)$$

where \mathbf{E} is the electric field. On the surface at $z = 0$, the current density is:

$$J_x = \cos \omega t \quad J_y = J_z = 0 \quad (31)$$

where $\mathbf{J} = (J_x, J_y, J_z)$ and ω is the frequency. The electric field will have the following form at depth z :

$$J_x(z) = e^{-z\sqrt{2\pi\sigma\omega}} \cos(\omega t - z\sqrt{2\pi\sigma\omega}) \quad J_y = J_z = 0 \quad (32)$$

It is important to note that with (32), we observe the skin effect, where as the depth increases, the exponential decreases while the phase retardation increases. It is thus useful to describe the distance known as the "skin depth", often represented as δ . This is the depth at which the amplitude of the electric field at the surface has decreased to the fraction e^{-1} . It is defined as:

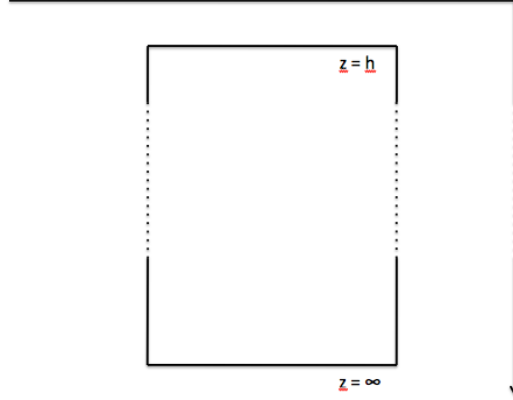
$$\delta = \frac{1}{\sqrt{2\pi\sigma\omega}} \quad (33)$$

We may also note that for every distance δ below the surface, the phase is retarded by one radian.

Now let us consider the magnetic field. Since the electric field dies off as z approaches infinity, the magnetic field must do the same. Recalling Ampère's Circuital Law:

$$\nabla \times \mathbf{H} = \mathbf{J} \quad (34)$$

where, \mathbf{H} is the magnetic H-field, let us consider a path to integrate, a rectangle with a side a distance z below the surface of the Earth, parallel to the surface, and a side infinitely below the surface, both connected by sides orthogonal to the surface:



The sides parallel to the surface must run along the y -axis, since we specified above that the amplitude of the magnetic field runs along this side. When applying Ampère's Circuital Law, (34), to this loop, we calculate \mathbf{H} :

$$H_y(z) = 4\pi \int_z^\infty J_x dz = 2\sqrt{\frac{\pi}{\sigma\omega}} e^{-z\sqrt{2\pi\sigma\omega}} \cos\left(\omega t - z\sqrt{2\pi\sigma\omega} - \frac{\pi}{4}\right)$$

$$H_x = 0 \tag{35}$$

Recalling the relationship between electric field and current density, thus combining (30), (32), and (35), it is important to note that the ratio between the amplitudes of the electric and magnetic field is:

$$\frac{E_x}{H_y} = \frac{1}{2}\sqrt{\frac{\omega}{\pi\sigma}} \tag{36}$$

while the phase retardation of the magnetic field relative to the electric field is $\frac{\pi}{4}$. Note that the resistivity is an inverse of conductivity, $\sigma = \rho^{-1}$. We may rearrange (36) to note how best to infer the resistivity of this assumed uniform Earth:

$$\rho = \frac{2\pi}{\omega} \left(\frac{E_x}{H_y}\right)^2 \tag{37}$$

This crucial result is the basis for the subsequent calculations. The Earth is not usually a uniform layer beneath the surface. In the case of sub-glacial water systems, the Earth consists of 3 layers, ice, sub-glacial water,

and bedrock, as illustrated in Figure 1. Thus, the above ρ is more of an apparent resistivity, which we will call ρ_a for the remainder of this paper, since it measures a weighted average of multiple layers. We can already begin to imagine how the above will be useful in inferring the structure of multiple layer of the Earth by considering the skin depth. As frequencies become lower (hence, the periods get higher), the skin depth increases. As the layers in the Earth change, lower frequencies begin to detect these changes. Since resistivity influences the skin depth and is part of this quotient between the amplitude of the electric and magnetic fields, layers of different resistivity will affect the amplitude. By taking this ratio of electric and magnetic fields, we receive information of the Earth below the surface's resistivity, primarily dictated by the distance between the surface of the Earth and the skin depth. By taking this ratio at various frequencies, we attain this information at various depths, and can create a profile of apparent resistivities, thus extracting the whole profile on the structure of the Earth below the surface and its layers.

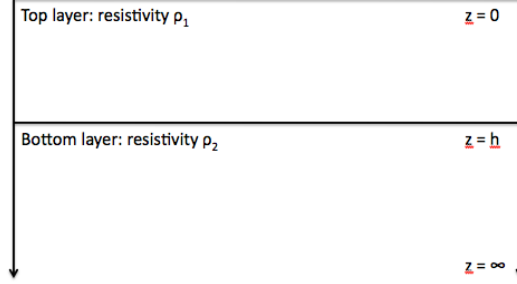
3.4 Magneto-telluric Results

This technique has been widely used for hydrocarbon and mining exploration in the past decades, yet its usefulness in detecting sub-glacial water has yet to be investigated. We continue our investigation below by calculating various forward models for potential structures of the sub-glacial water system. We begin by presenting a relatively straightforward 2-layer model, primarily to present the math and intuition behind the use of this technique, and show how the profile of apparent resistivities can lead us to extract a profile of the structure below the surface of the Earth in terms of resistivities. Then, we extend this to a 3-layer model incorporating the real model of ice, water, and bedrock, showing a practical, although mathematically more complex, profile. We then explain how to turn the field data into a profile of the underground structure.

3.4.1 The Two Layer Model

In this model, we consider two layers of material with resistivities ρ_1 and ρ_2 below the surface of the Earth, where the top of the first layer is a flat surface along the $z = 0$ plane. The point where the first surface meets the second surface is also flat, running along $z = h$. The following figure

illustrates this model:



Using the above model, we can work out the math behind creating a profile of this structure using the electric and magnetic fields at the surface. Let us say the electric and magnetic fields within the second layer of the Earth are as follows:

$$E_x = e^{i\omega t} e^{-\alpha\sqrt{\sigma_2}z}$$

$$H_y = 2\sqrt{\frac{\pi\sigma_2}{\omega}} e^{i\frac{\pi}{4}\omega t} e^{-\alpha\sqrt{\sigma_2}z} \quad (38)$$

where α is:

$$\alpha = 2\sqrt{\pi\omega} e^{-i\frac{\pi}{4}} \quad (39)$$

Since in the top layer of this model these electric and magnetic fields will contain both upwelling and downwelling contributions, the form of these fields in the top layer is:

$$E_x = e^{i\omega t} (Ae^{\alpha\sqrt{\sigma_1}z} + Be^{-\alpha\sqrt{\sigma_1}z})$$

$$H_y = 2\sqrt{\frac{\pi\sigma_1}{\omega}} e^{i\frac{\pi}{4}\omega t} (-Ae^{\alpha\sqrt{\sigma_1}z} + Be^{-\alpha\sqrt{\sigma_1}z}) \quad (40)$$

We may solve for A and B by applying the necessary boundary conditions at $z = h$ that assure continuity of the electric and magnetic fields:

$$Ae^{\alpha\sqrt{\sigma_1}h} + Be^{-\alpha\sqrt{\sigma_1}h} = e^{-\alpha\sqrt{\sigma_2}h}$$

$$-A\sqrt{\sigma_1}e^{\alpha\sqrt{\sigma_1}h} + B\sqrt{\sigma_1}e^{-\alpha\sqrt{\sigma_1}h} = \sqrt{\sigma_2}e^{-\alpha\sqrt{\sigma_2}h} \quad (41)$$

leading us to conclude that:

$$\begin{aligned} A &= \frac{\sqrt{\sigma_1} - \sqrt{\sigma_2}}{2\sqrt{\sigma_1}} e^{-\alpha h(\sqrt{\sigma_1} + \sqrt{\sigma_2})} \\ B &= \frac{\sqrt{\sigma_1} + \sqrt{\sigma_2}}{2\sqrt{\sigma_1}} e^{\alpha h(\sqrt{\sigma_1} - \sqrt{\sigma_2})} \end{aligned} \quad (42)$$

Recalling (37), we can find an expression for the ratio of the electric to magnetic fields more easily by rewriting them as follows:

$$E_x = C e^{i\omega t} e^{-i\phi}$$

$$H_y = 2\sqrt{\frac{\pi\sigma_1}{\omega}} D e^{i\omega t} e^{i(\pi/4 - \psi)} \quad (43)$$

where upon comparison of (43) with (38) through (42) and the use of some algebraic manipulation, we obtain the following relationships:

$$\begin{aligned} C \cos \phi &= \left(\frac{1}{\delta_1} \cosh \frac{h}{\delta_1} + \frac{1}{\delta_2} \sinh \frac{h}{\delta_1} \right) \cos \frac{h}{\delta_1} \\ C \sin \phi &= \left(\frac{1}{\delta_1} \sinh \frac{h}{\delta_1} + \frac{1}{\delta_2} \cosh \frac{h}{\delta_1} \right) \sin \frac{h}{\delta_1} \end{aligned} \quad (44)$$

$$\begin{aligned} D \cos \psi &= \left(\frac{1}{\delta_1} \sinh \frac{h}{\delta_1} + \frac{1}{\delta_2} \cosh \frac{h}{\delta_1} \right) \cos \frac{h}{\delta_1} \\ D \sin \psi &= \left(\frac{1}{\delta_1} \cosh \frac{h}{\delta_1} + \frac{1}{\delta_2} \sinh \frac{h}{\delta_1} \right) \sin \frac{h}{\delta_1} \end{aligned} \quad (45)$$

where we recall from (33) that δ is the skin depth, and note that δ_1 and δ_2 are the skin depths of the top and bottom layer respectively. We can now obtain the ratio of the electric to magnetic fields for the two-layer model:

$$\frac{E_x}{H_y} = \frac{1}{2} \sqrt{\frac{\omega}{\pi\sigma_1}} \frac{C}{D} e^{-i(\pi/4 + \phi - \psi)} \quad (46)$$

Ignoring the phase, however, and observing the magnitude of (46) and comparing it with (36), where we recall that for an arbitrary sub-surface structure

within the Earth, σ is actually σ_a the apparent conductivity, which is related to the apparent resistivity as $\sigma_a = \rho_a^{-1}$, we note that:

$$\rho_a = \rho_1 \left(\frac{C}{D} \right)^2 \quad (47)$$

Thus, to find the apparent resistivity, all we need to measure are the amplitudes of the electric and magnetic fields over a range of frequencies, and to directly measure the resistivity of the top layer of the Earth right at the surface. This means that we would have to measure the resistivity of the ice directly at the surface when we actually implement this technique. Since the skin depth is dependent on frequency, it is useful to note the following effects on ρ_a as the skin depth approaches 0 and ∞ :

$$\begin{aligned} \text{as } \delta \rightarrow 0 & \quad \rho_a \rightarrow \rho_1 \\ \text{as } \delta \rightarrow \infty & \quad \rho_a \rightarrow \rho_2 \end{aligned} \quad (48)$$

which are relationships easily attained by solving for C and D from (44) and (45) and then plugging in to (47).

Figure 6 shows the apparent resistivity of of the two-layer model as a function of period. In this model, we assume the top layer has a resistivity of $1 \Omega m$. The blue curve shows a model with a bottom layer of resistivity $0.1 \Omega m$, whereas the green and red have resistivities $0.02 \Omega m$ and $0.01 \Omega m$ respectively. The depth of the top layer is $1 km$. Since at low enough periods, the skin depth is so small, we simply measure the resistivity of the top layer. And at high enough periods, the skin depth is large, thus we measure the resistivity of the bottom layer. Since we have modeled each of these layer to have different resistivities, we notice a difference in the curves. The curve for the one layer model is simply a straight line in which the apparent resistivity is always equal to the actual resistivity of the layer. In order to get a glimpse of the profile one might actually see in the field, however, we must calculate the apparent resistivity as a function of period for the three-layer model.

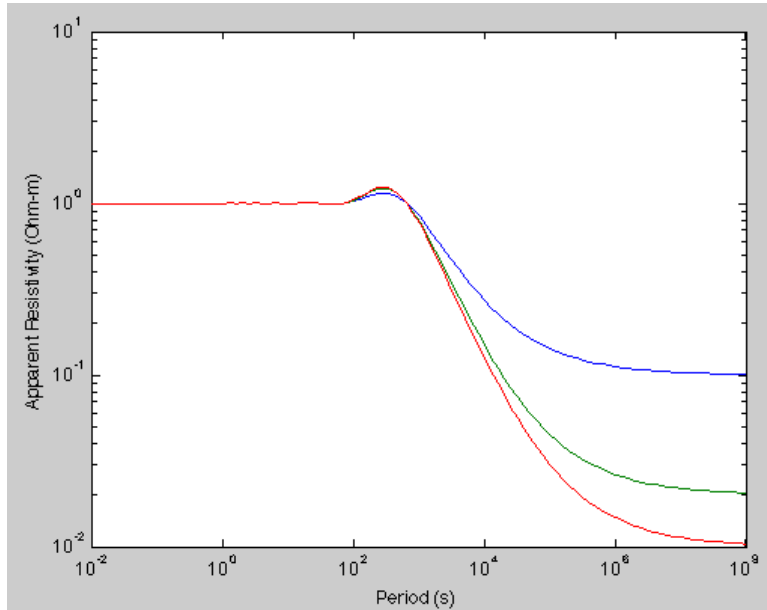
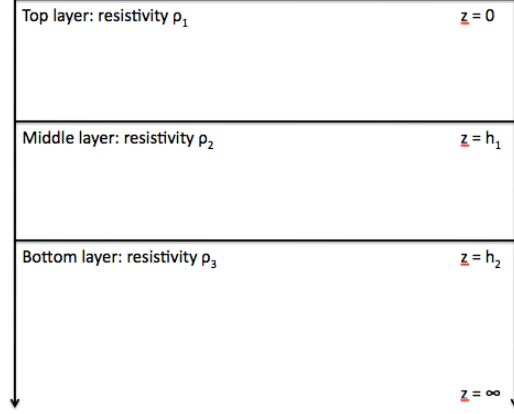


Figure 6: The above graphs show the apparent resistivity of of a two-layer model as a function of period. In this model, we assume the top layer has a resistivity of $1 \Omega m$. The blue curve shows a model with a bottom layer of resistivity $0.1 \Omega m$, whereas the green and red have resistivities $0.02 \Omega m$ and $0.01 \Omega m$ respectively. The depth of the top layer is $1 km$

3.4.2 The Three Layer Model

In this model, we consider three layers of material with resistivities ρ_1 , ρ_2 , and ρ_3 below the surface of the Earth, where the top of the first layer is a flat surface along the $z = 0$ plane. The point where the first surface meets the second surface is also flat, running along $z = h_1$. Finally, where the second surface meets the third surface, $z = h_2$. The figure below illustrates this model:



Solving for C and D in (46) for the three-layer model is more complex than that of the two-layer model. However, the approach is the same. Following the previous method, we obtain the following relationships between C , D , their respective phases, and the skin depths and heights of the layers:

$$\begin{aligned}
C \cos \phi &= \left(\frac{1}{\delta_1} - \frac{1}{\delta_2} \right) \left(\frac{1}{\delta_2} \cosh u - \frac{1}{\delta_3} \sinh u \right) \cos u \\
&\quad + \left(\frac{1}{\delta_1} + \frac{1}{\delta_2} \right) \left(\frac{1}{\delta_2} \cosh v + \frac{1}{\delta_3} \sinh v \right) \cos v \quad (49)
\end{aligned}$$

$$\begin{aligned}
C \sin \phi &= \left(\frac{1}{\delta_1} - \frac{1}{\delta_2} \right) \left(\frac{1}{\delta_2} \sinh u - \frac{1}{\delta_3} \cosh u \right) \sin u \\
&\quad + \left(\frac{1}{\delta_1} + \frac{1}{\delta_2} \right) \left(\frac{1}{\delta_2} \sinh v + \frac{1}{\delta_3} \cosh v \right) \sin v \quad (50)
\end{aligned}$$

$$\begin{aligned}
D \cos \psi &= \left(\frac{1}{\delta_1} - \frac{1}{\delta_2} \right) \left(\frac{1}{\delta_2} \sinh u - \frac{1}{\delta_3} \cosh u \right) \cos u \\
&\quad + \left(\frac{1}{\delta_1} + \frac{1}{\delta_2} \right) \left(\frac{1}{\delta_2} \sinh v + \frac{1}{\delta_3} \cosh v \right) \cos v \quad (51)
\end{aligned}$$

$$\begin{aligned}
D \sin \psi = & \left(\frac{1}{\delta_1} - \frac{1}{\delta_2} \right) \left(\frac{1}{\delta_2} \cosh u - \frac{1}{\delta_3} \sinh u \right) \sin u \\
& + \left(\frac{1}{\delta_1} + \frac{1}{\delta_2} \right) \left(\frac{1}{\delta_2} \cosh v + \frac{1}{\delta_3} \sinh v \right) \sin v
\end{aligned} \tag{52}$$

where we note that:

$$u = h_1 \left(\frac{1}{\delta_1} + \frac{1}{\delta_2} \right) - \frac{h_2}{\delta_2} \tag{53}$$

$$v = h_1 \left(\frac{1}{\delta_1} - \frac{1}{\delta_2} \right) + \frac{h_2}{\delta_2} \tag{54}$$

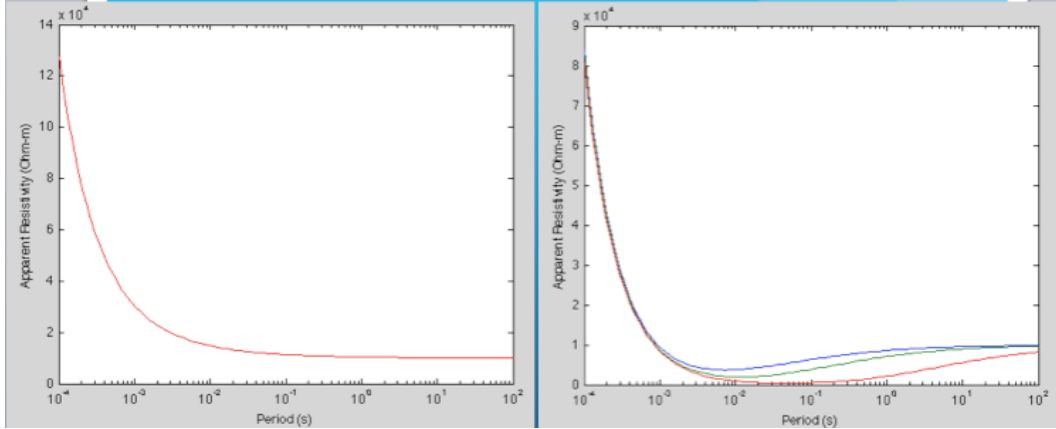


Figure 7: The above graphs show the apparent resistivity of a three-layer model as a function of period. In this model, we assume the top (ice) layer has a conductivity of $10^{-7} S/m$. The blue curve on the graph on the right shows a model with the middle (water) layer of conductivity $0.005 S/m$, whereas the green and red have conductivities $0.01 S/m$ and $0.05 S/m$ respectively. The depth of the top layer is $1 km$ and the depth of the water layer is $100 m$. In the graph on the left, however, we assume no water to show what we would detect if the ice were laying directly atop rock.

Figure 7 above shows the apparent resistivity of of a three-layer model as a function of period. In this model, we assume the top (ice) layer has a conductivity of $10^{-7} S/m$. The blue curve on the graph on the right shows a model with the middle (water) layer of conductivity $0.005 S/m$, whereas the green and red have conductivities $0.01 S/m$ and $0.05 S/m$ respectively. The depth of the top layer is $1 km$ and the depth of the water layer is 100

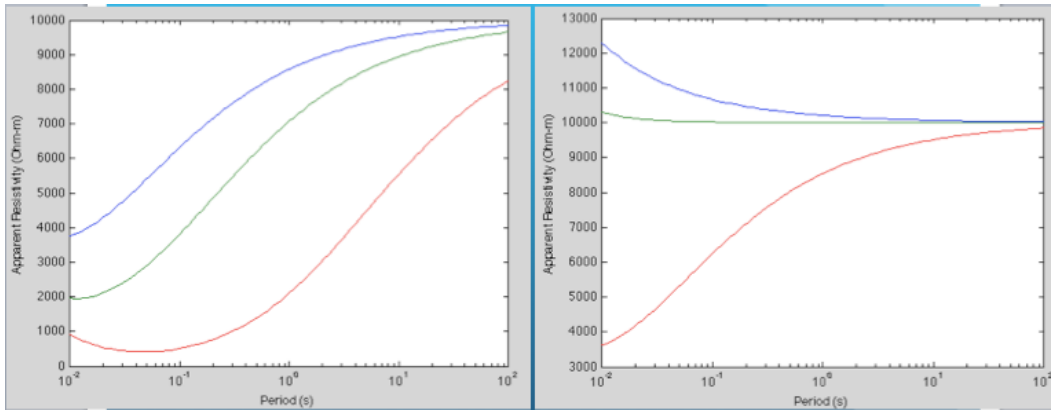


Figure 8: The above graphs show the apparent resistivity of of a three-layer model as a function of period, where we have zoomed in on the area of interest. In this model, we assume the first (ice) layer has a conductivity of $10^{-7} S/m$. The blue curve on both graphs show a model with a middle (water) layer of conductivity $0.005 S/m$, whereas the green and red have conductivities $0.01 S/m$ and $0.05 S/m$ respectively. The bottom (bedrock) layer has conductivity $10^{-4} S/m$. The depth of the top layer is $1 km$ and the depth of the water layer is $100 m$ for the figure on the left and $10 m$ for the figure on the right.

m . In the graph on the left, however, we assume no water to show what we would detect if the ice were laying directly atop rock. When there is water present, we notice a distinct difference in our measured apparent resistivity, alerting us to this presence. Thus, using this technique of magneto-tellurics, we can easily detect large bodies of water between the ice and bedrock. In fact, even with water layers on the order of a meter or 10s of centimeters, we still notice distinct differences between the curves.

Figure 8 below shows the apparent resistivity of of a three-layer model as a function of period, where we have zoomed in on the area of interest. In this model, we assume the first (ice) layer has a conductivity of $10^{-7} S/m$. The blue curve on both graphs show a model with a middle (water) layer of conductivity $0.005 S/m$, whereas the green and red have conductivities $0.01 S/m$ and $0.05 S/m$ respectively. The bottom (bedrock) layer has conductivity $10^{-4} S/m$. The depth of the top layer is $1 km$ and the depth of the water layer is $100 m$ for the figure on the left and $10 m$ for the figure on the right. We notice from this model that at smaller depths, it becomes more difficult to detect the water, as we would expect. However, even when the conductivity of this water is low, we can detect slight differences. Thus, even smaller depths of water might be realistically detectable, assuming a high enough conductivity. So long as the water is more conductive than the bedrock

below, we are immediately alerted of its presence by the large bending of the curve below that resistivity of the rock at these intermediate frequencies.

4 Discussion and Conclusions

When it came to magnetic induction, detecting the presence of water is a real possibility. We noted that thin sheet-like water layers on the order of a centimeter can realistically be detected by 1 *s* periods. The typical ratio of the internal to external magnetic fields are on the order of 10^{-1} , which is an order modern, cheap magnetometers can easily detect given the amplitude of naturally occurring magnetic fields in the ionosphere. Deeper water layers can be detected using naturally-varying external fields of longer periods. Magnetometers can easily detect variations of the order of seconds or more. Thus, the deeper the water, the easier to detect. However, when we attempted to measure the variability in the water layers in the sinusoidal and Gaussian channel models, the technique is not so feasible given modern, cheap magnetometers and the naturally occurring magnetic fields in Earth's ionosphere. We noted that we like the ratio of *b* to *F* to be on the order of 10^{-1} , and we noted that only when we have a water layer with the huge 100 *km* wavelength in variability are we able to easily detect this variability. One order of magnitude less and might need the variability in a magnetic storm to detect this variability. Thus, detecting the variability we look for on the order of 1 *m* is not feasible using this technique.

When it came to magneto-tellurics, detecting the presence of even small depths of water was very feasible. We noted that we can easily detect large bodies of water between the ice and bedrock. In fact, even with water layers on the order of a meter or 10s of centimeters, we still notice distinct differences between the curves we create of the apparent resistivity of the ground while measuring the naturally occurring magnetic and electric fields within the surface of the Earth. One disadvantage of the magneto-telluric technique is that we need the presence of both magnetometers and voltmeters to detect both the electric and magnetic fields. However, the naturally occurring currents are very straightforward to detect, and detecting them over a range of periods gives more certainty to the shape of the curve and thus the exact nature of the depth and conductivity of the water beneath, whereas the magnetic induction technique can only measure the product of the depth and conductivity.

5 Future Directions

We have already established that using the magnetic induction technique is not feasible for detecting the variability in most sub-glacial water systems. However, using the results of the Gaussian channel model, it should be feasible to detect the presence of sub-glacial lakes and to note how large they are, such as Lake Vostok. It would be useful to attain some magnetic data from the Antarctic region to find out whether or not the actual implementation of this method was able to detect not only the presence of Lake Vostok by finding the product of its depth and conductivity, but also its approximate length.

The model used for magneto-tellurics was limited only to detecting the presence of water, which we already established as possible with magnetic induction. However, no investigation was conducted on whether or not it would be feasible to detect the variability in the water. We predict it would be more feasible since we are gathering data from not merely the magnetic field, but also the electric field. However, an actual calculation of this theoretical model must be conducted before we can verify this assumption. Should this prove to be a feasible way of detecting the variability, then investigation must be conducted on how to actually implement the technique in the field.

References

- Arendt, A.A., Echelmeyer, K.A., Harrison, W.D., Lingle, C.S., and Valentine, V.B., (2002), Rapid Wastage of Alaska Glaciers and Their Contribution to Rising Sea Level, *Science*, Vol. 297 no. 5580 pp. 382–386 DOI: 10.1126/science.1072497.
- Cagniard, L. (1953) Basic theory of the magneto-telluric method of geophysical prospecting, *Geophysics*, 18, 605635.
- Cox, R.A., McCartney, M.J., Culkin, F. (1970), The Specific Gravity/Salinity/Temperature Relationship in Natural Sea Water, *Deep Sea Research and Oceanographic Abstracts*, 17(4), 679–689.
- Das, S., I. Joughin, M. Behn, I. Howat, M. King, D. Lizarralde, and M. Bhatia, (2008), Fracture propagation to the base of the Greenland Ice Sheet during supraglacial lake drainage, *Science*, 320, 778–781, doi:10.1126/science.1153360.
- Farquharson, C.G., Craven, J.A. (2009), Three-Dimensional Inversion of Magnetotelluric Data for Mineral Exploration: An Example from the McArthur River

Uranium Deposit, Saskatchewan, Canada, *Journal of Applied Geophysics*, 68(4), 450–458.

Fowler, A.C. (1979), A mathematical approach to the theory of glacier sliding, *Journal of Glaciology*, 23(89), 131–141.

Fowler, A.C., (1986), Sub-temperate basal sliding, *Journal of Glaciology*, 32(110), 3–5.

Gordon, S., M. Sharp, B. Hubbard, I. Willis, C. Smart and B. Ketterling, (1998), Seasonal reorganization of subglacial drainage inferred from measurements in boreholes. *Hydrological Processes* 12, 105–133. ISSN: 0885–6087.

Iken, A. and R.A. Bindschadler, (1986) Combined measurements of subglacial water pressure and surface velocity of Findelengletscher, Switzerland: Conclusions about drainage system and sliding mechanism, *Journal of Glaciology*, 32(110), 101–119.

Iken, A., (1981), The effect of subglacial water pressure on the sliding velocity of a glacier in an idealized numerical model, *Journal of Glaciology*, 27(97), 407–422.

Kamb B., (1987), Glacier surge mechanism based on linked-cavity configuration of the basal water conduit system. *Journal of Geophysical*, 92(B9), 9083–9100.

Kamb, B., (1970), Sliding motion of glaciers: theory and observation, *Reviews of Geophysics* 8(4), 673–728.

Kaser, G., Cogley, J.G., Dyurgerov, M.B., Meier, M.F., and Ohmura, A., (2006), Mass Balance of Glaciers and Ice Caps: Consensus Estimates for 1961–2004. *Geophysical Research Letters*, Vol. 33, L19501, doi:10.1029/2006-GL027511.

Kulesa, B., (2007), A Critical Review of the Low-Frequency Electrical Properties of Ice Sheets and Glaciers. *J. Environ. Eng. Geophysics*, 12(1), 23–36.

Orange, A.S. (1989), Magnetotelluric Exploration for Hydrocarbons, *Proceedings of the IEEE*, 77(2), 287–317.

Pedersen, L.B., Bastani, M., Dynesius, L. (2005), Groundwater Exploration Using Combined Controlled-Source and Radiomagnetotelluric Techniques, *Geophysics*, 70(2), p. G8–G15. doi: 10.1190/1.1852774.

Price, A.T., (1949), The induction of electric currents in non-uniform thin sheets and shells. *Quarterly Journal of Mechanics and Applied Mathematics*, 2: 283–310.

Seaton, W.J., Dean, T. (2004), Engineering Site Characterization with Electrical Resistivity Surveys. *American society for Trenchless Technology*. ATS International, Inc., Christiansburg, VA.

Stearns, L.A., B.E. Smith and G.S. Hamilton, (2008), Increased flow speed on a large East Antarctic outlet glacier caused by subglacial floods. *Nature Geosci.*, 1(12), 827–831.

Stepisnik, J. (2006), Spectroscopy: NMR Down to Earth, *Science*, 439, 799–801.

Volpi, G., Manzella, A., Fiordelisi, A. (2003), Investigation of Geothermal Structures by Magnetotellurics (MT): An Example from the Mt. Amiata Area, Italy. *Geothermics*, 32(2), 131–145.

Zimmer, C., Khurana, K.K., Kivelson, M.G., (2000), Subsurface Oceans on Europa and Callisto: Constraints from Galileo Magnetometer Observations. *Icarus*, 147, 329–347.

Zwally, H., W. Abdalati, T. Herring, K. Larson, J. Saba, and K. Steffen, (2002), Surface melt-induced acceleration of Greenland Ice-Sheet flow, *Science*, 297(5579), 218–222.